ISSN 2075-1087, Gyroscopy and Navigation, 2024, Vol. 15, No.1, pp. 69-83
Russian Text © The Author(s), 2024, published in Giroskopiya i Navigatsiya, 2024, No. 1, pp. 94-114

Clock Bias Gross Error Detection Method Based on WS-MAD

Jia Su [a], Mengjia Gao [a], Qingwu Yi [b,*], Binbin Wang [b], and Zhiwei Ma [c]

[a] *College of Information Science and Engineering, Hebei University of Science and Technology, Shijiazhuang, China*
[b] *State Key Laboratory of Satellite Navigation System and Equipment Technology, Shijiazhuang, China*
[c] *Henan University of Economics and Law, Zhengzhou, China*

**e-mail: 13933827718@139.com*

Received December 18, 2023; reviewed February 27, 2024; accepted April 10, 2024

Abstract: This paper proposes a clock bias gross error detection method, which combines weighted support vector data description (SVDD) with modified median absolute deviation (MAD) to address the limitations of the traditional MAD method. The method uses the local reachable density as the weighting factor of SVDD, which fully considers the local characteristics of each data. By constructing the minimum hypersphere in the high-dimensional feature space, the one-dimensional data are transformed into the distance from the vector point to the center of the hypersphere in the high-dimensional space. This transformation increases the discrepancy between normal data and gross errors. The modified MAD method probes the distance from the current epoch vector point to the center of the hypersphere for gross errors, and thus determines whether the current clock bias is a gross error. The precision clock bias data of BDS-3 with different sampling intervals provided by GFZ were used for simulation experiments. By comparing the results of the MAD method and the WS-MAD method, it is found that the WS-MAD method can detect the small gross errors in the smooth clock bias frequency data and more gross errors in the clock bias data with trend term floating. The fitting and prediction analyses on satellites with different orbits and clock types show that the WS-MAD method improves the fitting and prediction accuracy of MEO and IGSO satellites better than that of GEO satellites. For the same MEO satellites, the enhancement effect of hydrogen clocks is better than that of rubidium clocks.

Keywords: satellite clock bias; gross error detection; weighted SVDD; MAD; satellite clock bias prediction.

1. INTRODUCTION

Precision clock bias data of GNSS satellites serve as the foundation for performance analysis of spaceborne atomic clocks, as well as for modeling and predicting satellite clock bias [1]. However, due to operations such as clock switching, phase or frequency tuning during satellite high-speed movement, as well as external environmental interference and internal factors, calculated clock bias data often contains gross errors, jumps, and missing data. Thus, reasonable and effective data preprocessing is necessary for satellite clock research, as it is crucial for ensuring the reliability of research results [2].

Currently, various effective strategies and processing methods exist for addressing abnormal situations such as jumps and data discontinuities [3]. Zhou et al. proposed an algorithm to find the jump point of clock bias data by using a moving window [4]; Guo proposed a clock bias jump detection based on the Hilbert-Huang transform [5]; Ghaderpour et al. gave the processing method of unequal interval data [6]; Riley and Howe propose a time-domain Allan variance divided by the Barnes deviation function to deal with data discontinuities [7]. For the gross error problem, Wang made use of the multi-resolution characteristics of wavelet analysis to carry out a preliminary discussion on the application of this method in the gross error processing of atomic clock data [8]; Fang studied the application of cluster analysis in multivariate statistical methods in the gross error detection of satellite clock bias [9]; Wei proposed a median line gross error detection method for the linear trend of primary differential data [10]; Zhang et al. proposed a method for detecting the gross error of satellite-ground time synchronization clock bias based on Bayesian principle [11]. The most commonly used traditional gross error detection method is median absolute deviation (MAD) [12]. While it is simple and has low computational complexity, its effectiveness in detecting outliers of smaller magnitude in clock bias

is limited due to the reliance on empirical thresholds. Additionally, its ability to process clock bias frequency data with trend terms is also limited.

In recent years, Support Vector Data Description (SVDD) and its extended algorithms have gained popularity in the field of anomaly detection, with related theories finding wide application [13]. An important step in SVDD modeling is to project the data into a high-dimensional feature space. This approach can handle nonlinear problems and does not require data to conform to a strict Gaussian distribution [14].

This study employs SVDD to model clock bias frequency data by mapping it from the original space to a higher dimensional feature space, where a minimum hypersphere is constructed. The clock bias frequency data is transformed into the distance from the sample point to the center of the hypersphere, increasing the differentiation between normal and gross error data. Considering that all sample points are equally important for model construction, making the model insensitive to outliers and data density, the local reachable density is introduced to weight the SVDD model [15]. The local reachable density covers more neighborhood information than traditional density, enabling better extraction of local features in frequency data and easier differentiation between normal and gross error points. Using Beidou Global Navigation Satellite System (BDS-3) satellites with different orbits and clock types, this study analyzes the feasibility and superiority of the improved algorithm in terms of gross error elimination, fitting accuracy, and prediction accuracy.

Next, the weighted SVDD as well as the modified MAD methods are explained and then the experimental results are shown. In addition, the results are compared and described in detail. Conclusions are given in the last part.

2. WS-MAD CLOCK BIAS GROSS ERROR DETECTION METHOD

2.1. LRD Weighted SVDD

The idea of SVDD is to construct a minimum-volume hypersphere in a high-dimensional space that contains all normal data samples and excludes outliers from the hypersphere [16]. In the SVDD modeling process, the initial data $Y=[y_1,y_2,\ldots,y_N]^T$, $y_i\in\mathbb{R}$, $i=1,2,\ldots N$, where N is total number of data and Y is first normalized by:

$$\overline{Y}(i)=\frac{Y(i)-\hat{Y}}{\sigma}, \tag{1}$$

where $\overline{Y}=[\overline{y}_1,\overline{y}_2,\ldots,\overline{y}_N]^T$, $\overline{Y}(i)$ is equivalent to $\overline{y}_i$, $\hat{Y}$ is the mean of the sample data, and σ is the variance. Then, the data is mapped to the higher-dimensional feature space through the nonlinear transformation function $\Phi(\cdot)$. Here we have used the Gaussian kernel function.

In traditional SVDD, each data is given equal importance in model construction, which can cause insensitivity to gross errors and data density. To address this issue, weighted SVDD introduces weighting factors for each data to improve the compactness of the model. Unlike traditional SVDD, weighted SVDD solves the following equation to compute the corresponding hyperspheres:

$$\begin{aligned}&\min_{R,a,\xi} R^2+C\sum_{i=1}^{N}w_i\xi_i\\&s.t\left\|\Phi(\overline{y}_i)-a\right\|\le R^2+\xi_i,\xi_i\ge 0,\end{aligned} \tag{2}$$

Where a and R are the center and radius of the hypersphere, respectively; $C=(1/(p\times N))$ is a trade-off parameter, p is the probability that normal data are allowed to be misreported as outliers in the data [17]; ξ_i is a slack variable that allows the existence of anomalies outside the hypersphere, w_i is the weight of the i-th data, and its smaller value indicates that the corresponding data is more likely to be an outlier.

In the process of training the model, the weight factors of weighted SVDD ought to adequately represent the local distribution features of each data. Density serves as a significant metric for evaluating data distribution and has been widely utilized in the formulation of weighting factors. One of these metrics is the Local Reachability Density (LRD) [18], which takes into account not only the distance between a data point and its neighbors but also the neighborhood information of its neighbors.

Compared to traditional density, the Local Reachability Density encompasses a broader range of neighborhood information. This information is incorporated into the weights of the SVDD model to enhance the extraction of local features from data points. The specific steps involved are as follows [19]:

Step 1: Find the K nearest neighbors of the data $\overline{y}_i$ to form its local neighbor set $LN(\overline{y}_i)$.

Step 2: In the local neighbor set $LN(\overline{y}_i)$, define the radius as $K-\text{distance}(\overline{y}_i)$.

$$\begin{aligned} &K-\text{distance}(\overline{y}_i)= \\ &=\max\{\overline{y}_j\in LN(\overline{y}_i)\,|\,ED(\overline{y}_i,\overline{y}_j)\} \end{aligned} \quad (3)$$

where $ED(\overline{y}_i,\overline{y}_j)=\sqrt{(\overline{y}_i-\overline{y}_j)^2}$ denotes the Euclidean distance between $\overline{y}_i$ and $\overline{y}_j$.

Step 3: Calculate the Euclidean distance between $\overline{y}_i$ and $\overline{y}_i^k\,(k=1,2,...,K)$, where $\overline{y}_i^k$ is the

k-th nearest neighbor of $\overline{y}_i$. Then, relative to $\overline{y}_i^k$, the reachable distance of $\overline{y}_i$ is calculated as:

$$\begin{aligned} &reach\_d(\overline{y}_i,\overline{y}_i^k)= \\ &=\max\{K-\text{distance}(\overline{y}_i^k),d(\overline{y}_i,\overline{y}_i^k)\} \end{aligned}, \quad (4)$$

where $d(\overline{y}_i,\overline{y}_i^k)$ denotes the Euclidean distance between $\overline{y}_i$ and $\overline{y}_i^k$.

From Eq. (3), it can be seen that the reachable distance of $\overline{y}_i$ is not only related to its direct neighbor $\overline{y}_i^k$, but also to the K-nearest neighbors of its neighbor.

Finally, the local reachable density is inversely proportional to the reachable distance, which is defined as:

$$LRD(\overline{y}_i)=\frac{K}{\sum_{k=1}^{K}reach\_d(\overline{y}_i,\overline{y}_i^k)}. \quad (5)$$

After introducing the LRD weighting factor, the weighted SVDD modeling process is executed and Eq. (2) may be converted into the following equation through introducing the Lagrange multipliers $\alpha=[\alpha_1,\alpha_2,\ldots,\alpha_N]^T$

$$\begin{aligned} &\min_{\alpha_i}\sum_{i=1}^{N}\alpha_i Ker(\overline{y}_i,\overline{y}_i)-\sum_{i=1}^{N}\sum_{j=1}^{N}\alpha_i\alpha_j Ker(\overline{y}_i,\overline{y}_j) \\ &s.t.\sum_{i=1}^{N}\alpha_i=1, 0\le\alpha_i\le w_i C \end{aligned}, \quad (6)$$

where $Ker(\overline{y}_i,\overline{y}_i)=\left\langle\Phi(\overline{y}_i)\cdot\Phi(\overline{y}_j)\right\rangle=e^{[-(\overline{y}_i-\overline{y}_j)^T(\overline{y}_i-\overline{y}_j)/\sigma^2]}$ is the kernel function [20], and after solving Eq. (6), only the object $\overline{y}_i$ with $\alpha_i>0$ is called support vectors (SVs), and its subscript set is $SV=\{i\,|\,\alpha_i>0, i=1,2,\ldots,N\}$. Compared with the traditional SVDD method, the upper limit of the constraints in Eq. (2) becomes $w_i C$. Equation (6) is still a quadratic optimization problem, and finally, the center a and radius R of the hypersphere are:

$$a=\sum_{i\in sv}\alpha_i\Phi(\overline{y}_i) \quad (7)$$

$$R=\sqrt{Ker(\overline{y}_{sv},\overline{y}_{sv})-2\sum_{i=1}^{N}\alpha_i Ker(\overline{y}_{sv},\overline{y}_i)+\sum_{i=1}^{N}\sum_{j=1}^{N}\alpha_i\alpha_j Ker(\overline{y}_i,\overline{y}_j)}. \quad (8)$$

This gives the distance from each sample point to the center of the hypersphere:

$$Dist(\overline{y}_i)=\sqrt{Ker(\overline{y}_i,\overline{y}_i)-2\sum_{i=1}^{N}\alpha_i Ker(\overline{y}_i,\overline{y}_i)+\sum_{i=1}^{N}\sum_{j=1}^{N}Ker(\overline{y}_i,\overline{y}_j)}. \quad (9)$$

2.2 Modified MAD gross error detection method

Typically, the original satellite clock bias data exhibits a large magnitude, making it difficult to identify the easily concealing abnormal points. Therefore, the detection of gross errors in clock bias data is commonly performed using its corresponding frequency data [21]. The magnitude of frequency data is small, and the gross error point corresponding to its peak value is easy to detect. The correspondence between the clock bias (phase) data and frequency data is as follows [22]:

$$y_i=\left(x_{i+1}-x_i\right)/\tau_0, \quad (10)$$

where y_i is the frequency value of the i-th epoch; x_{i+1} and x_i are the clock bias values of the $i+1$ and i epochs, respectively; τ_0 is the time interval between adjacent epochs; $i=1,2,3\ldots N$.

The idea of the MAD method is [23]: compare the frequency data y_i with the sum of the median m and

several multiples of the Median Absolute Deviation (MAD) in the frequency data sequence. If the clock bias frequency data satisfies Eq. (11), it is considered to be a gross error point and the value should be eliminated.

$$|y_i| > (m + nMAD), \tag{11}$$

where $m = median\{y_i\}$, $MAD = median\{|y_i - m|/0.6745\}$ and n is an integer, generally taking the empirical value of 3.

In Eq. (11), y_i is the clock bias frequency data, the left term $|y_i|$ denotes the absolute value of the clock bias frequency data, and MAD is positive in the right term. $nMAD$ can be regarded as a variable with constant positive value, when the right term $m + nMAD < 0$, y_i is judged as a gross error, which shows that the mathematical expression of the traditional MAD model is ambiguous. The MAD algorithm judges whether the distance of each y_i deviating from the median is limited. When the left term is $|y_i - m|$, its mathematical meaning is the distance y_i deviating from the median m. Similarly, when the right hand side is $nMAD$, its mathematical meaning is to determine whether y_i is the threshold distance value of gross error. Therefore, the traditional MAD method is modified to [24]:

$$|y_i - m| > nMAD. \tag{12}$$

After the gross error is detected, it is complemented by linear interpolation.

2.3 WS-MAD methodology flow

The weighted SVDD with modified MAD method is referred to as the WS-MAD method. The flow chart of the WS-MAD gross error detection method is shown in Fig. 1. The specific process is as follows.

Step 1: The original clock bias data $X = \{x_1, x_2, \ldots x_{N+1}\}$, $x_i \in \mathbb{R}$, $i = 1, 2, \ldots N+1$ are converted to clock bias frequency data $Y = \{y_1, y_2, \ldots y_N\}$, $y_i \in \mathbb{R}$, $i = 1, 2, \ldots N$ by Eq. (10).

Step 2: $\overline{Y}$ is obtained by normalizing $Y = [y_1, y_2, \ldots, y_N]^T$ according to Eq. (1).

Step 3: Based on the LRD method, the weight W of each data in $\overline{Y}$ is calculated.

Step 4: The weighted SVDD model is constructed using the weighting factor W. The center *a* of the corresponding hypersphere is calculated by solving Eq. (7).

Step 5: Calculate the distance Dist from the sample point to the center of the hypersphere. Then, bring the Dist set into Eq. (12) for judgment. If $|Dist - m| > nMAD$, then Dist is judged to be gross error, and the frequency data corresponding to the current epoch is judged to be gross error.

Step 6: After the gross error is removed, linear interpolation completes the data and converts the frequency data to clock bias phase data.

In this paper, the identification of gross error points diverges from the conventional approach of assessing whether sample points reside inside or outside the hypersphere. Instead, the one-dimensional clock bias frequency data is transformed into distances from sample points to the center of the hypersphere in a high-dimensional feature space using SVDD. Subsequently, the presence of gross errors within the frequency data is determined by examining the set of distances. The introduction of LRD to construct the weight factor of SVDD makes it easier to recognize the gross error by extracting the local features of the data points.

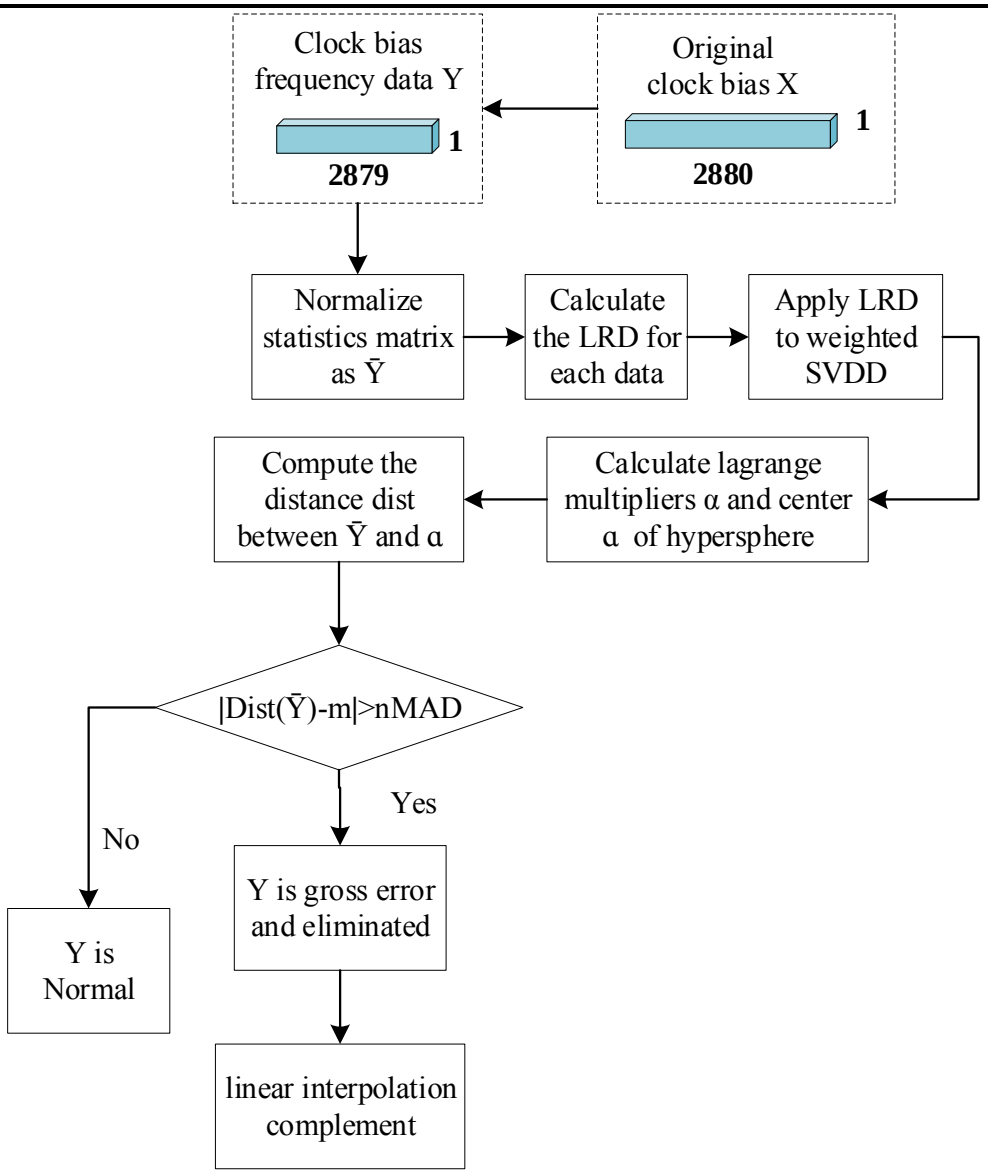

Fig. 1. Flowchart of the WS-MAD gross error detection scheme.

3. TEST COMPUTATION AND ANALYSIS

The experimental data are precision clock bias products of the BDS-3 system provided by the German Research Center for Geosciences (GFZ). Figure 2 gives the single-day clock bias data of four satellites with clock sampling intervals of 30 s and 300 s, respectively. At the same time, these four satellites cover three types of BDS-3 orbits and two types of clocks.

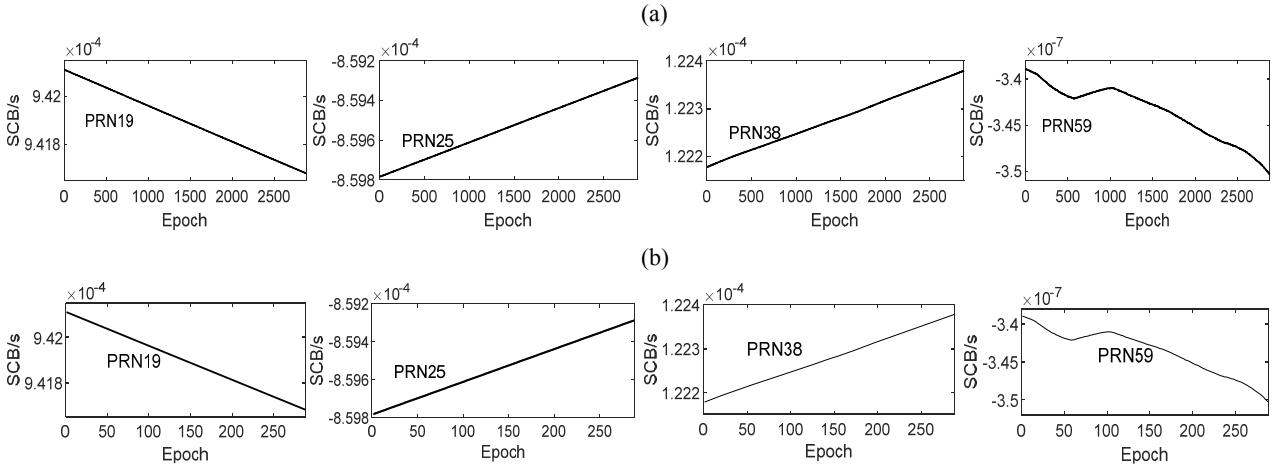

Fig. 2. BDS-3 original satellite clock bias sequence diagram of different orbits: (a) 30 s sampling interval; (b) 300 s sampling interval.

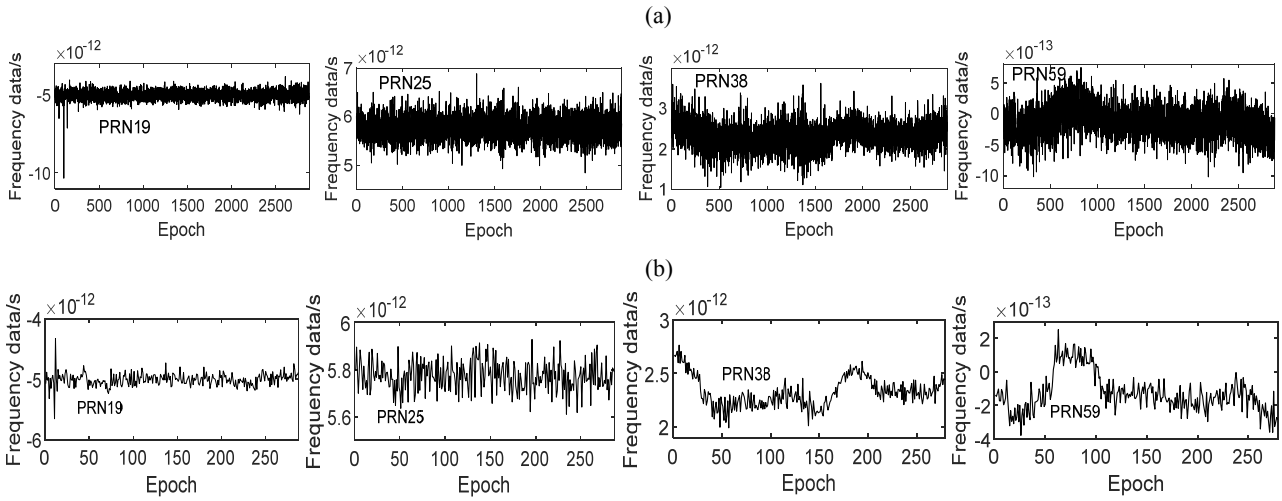

Fig. 3. BDS-3 clock bias frequency sequence for satellites in different orbits: (a) 30 s sampling interval; (b) 300 s sampling interval.

In Fig. 2, the clock bias sequence plots of the four satellites with different sampling intervals have the same data trend. PRN19 and PRN25 are BDS-3 medium earth orbit (MEO) satellites, PRN38 is BDS-3 inclined geosynchronous orbit (IGSO) satellite, and PRN59 is BDS-3 geostationary orbit (GEO) satellite. The overall trend can be seen through the satellite clock bias sequence diagram. The clock bias sequence diagrams for PRN19, PRN25, and PRN38 exhibit a linear trend, while the clock bias sequence diagram for PRN59 shows a phase jump and does not exhibit a linear trend. This phenomenon may be attributed to the introduction of orbit accuracy uncertainty in the GEO satellite, leading to reduced accuracy in the clock bias of PRN59 [25]. Additionally, it should be noted that the original clock bias sequence for the four satellites is on the order of microseconds (us), while the gross errors typically present in the clock bias are on the order of nanoseconds (ns). Therefore, gross errors should not be detected. The commonly employed approach involves dividing the original clock bias sequence by the sampling interval to convert it into clock bias frequency data, as depicted in Fig. 3.

Figure 3 clearly illustrates the presence of gross errors after converting the original clock bias data into frequency data. The frequency data with 300 s sampling interval have more obvious trend than the frequency data with 30 s sampling interval. Compared with the smooth frequency data series, the frequency data with obvious trend terms increase the difficulty of identifying the gross error. Utilizing clock bias data for modeling and forecasting without adequate error elimination will undoubtedly result in significant negative impacts, underscoring the importance of acquiring clean clock bias data [26].

Tables 1 and 2 present the results of gross error detection for the four satellites using two sample interval frequency data, with n values ranging from 1 to 5.

Table 1. Statistics of gross error detection values for four satellites (30 s)

Method	Satellite			
	PRN19	PRN25	PRN38	PRN59
MAD1	865	897	912	933
MAD2	97	117	145	134
MAD3	8	10	22	9
MAD4	3	1	0	0
MAD5	2	0	0	0

Table 2. Statistics of gross error detection values for four satellites (300 s)

Method	Satellite			
	PRN19	PRN25	PRN38	PRN59
MAD1	96	86	97	101
MAD2	14	9	20	48
MAD3	4	0	1	13
MAD4	2	0	0	1
MAD5	2	0	0	0

Analysis of Tables 1 and 2 reveals that an increase in the value of n corresponds to a higher number of detected gross errors. Ideally, gross errors should constitute a small portion, typically no more than ten percent of the dataset. The value n is usually taken to be 3 when MAD gross errors are detected.

3.1. Experiment 1

For the convenience of description, the modified MAD method used in the subsequent experiments will be referred to as the MAD method. The MAD

method and the WS-MAD method proposed in this paper are utilized to detect the gross errors in the clock bias frequency data of the four satellites PRN19, PRN25, PRN38, and PRN59 with sampling intervals of 30 s and 300 s. The detection results are shown in Figs. 4 and 5. In the figures, the gross errors identified by the MAD method are denoted by blue solid points, while the gross errors detected by the WS-MAD method are depicted using red circles.

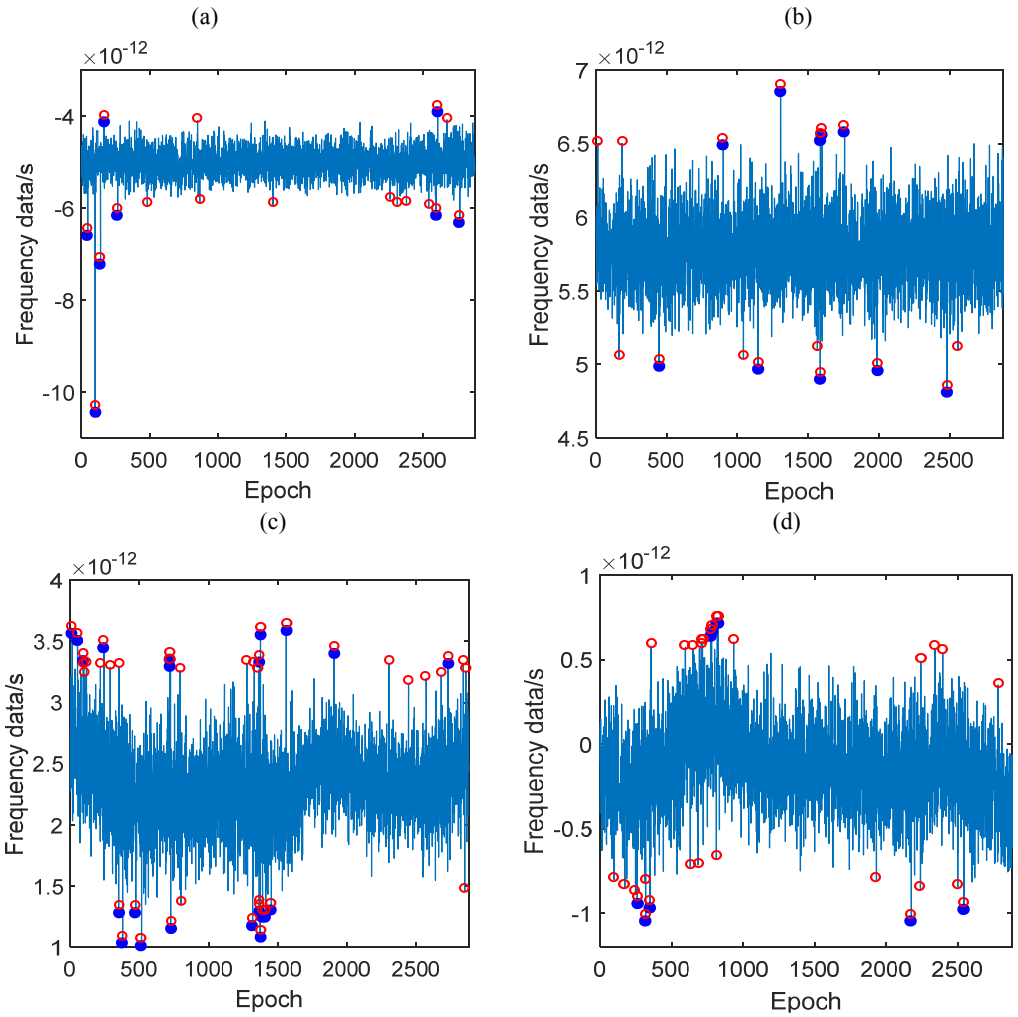

Fig. 4. Four satellites based on MAD and WS-MAD gross error detections (30 s): (a) PRN19 (BDS-3 MEO); (b) PRN25 (BDS-3 MEO); (c) PRN38 (BDS-3 IGSO); (d) PRN59 (BDS-3 GEO).

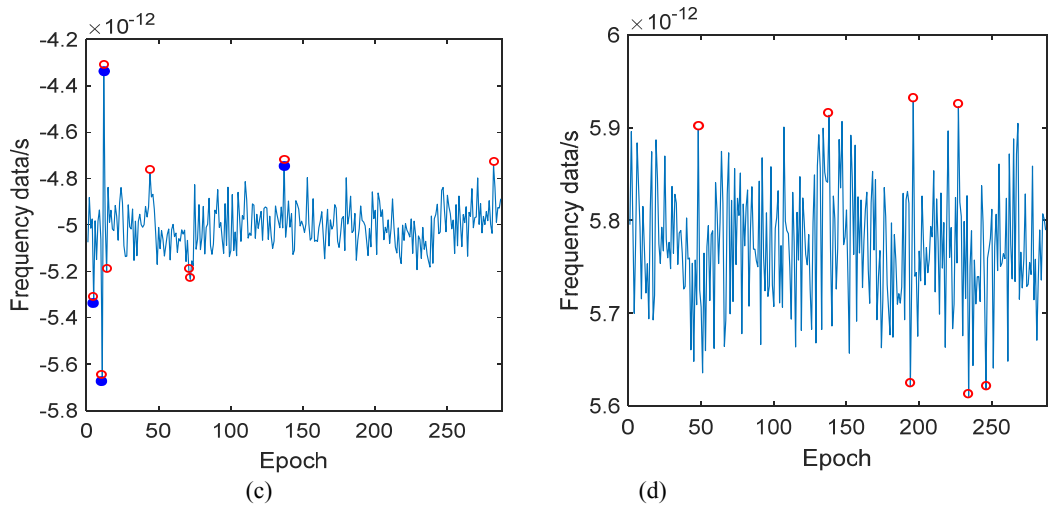

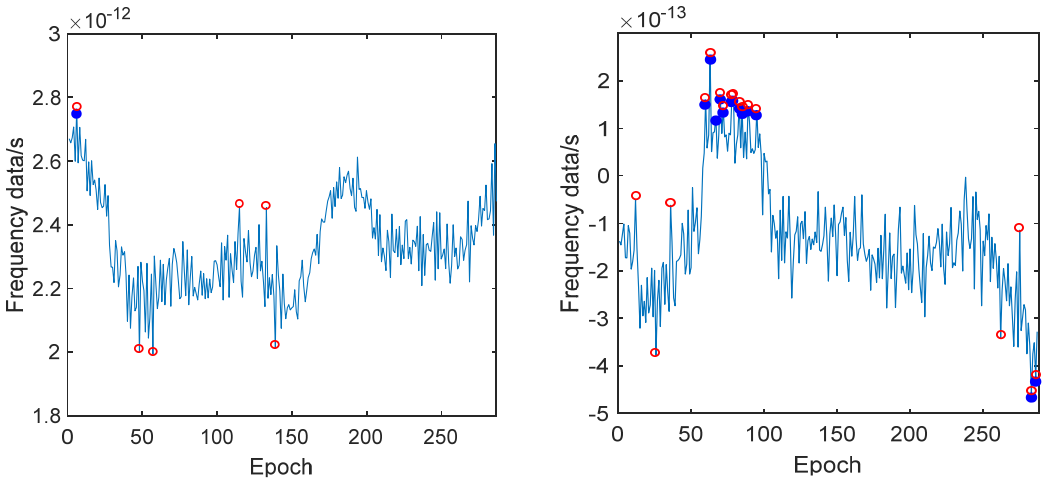

Fig. 5. Four satellites based on MAD and WS-MAD gross error detections (300 s) (a) PRN19 (BDS-3 MEO); (b) PRN25 (BDS-3 MEO); (c) PRN38 (BDS-3 IGSO); (d) PRN59 (BDS-3 GEO).

Additionally, Table 3 presents the count of gross errors detected by both methods for sampling intervals of 30 s and 300 s.

Table 3. Statistics of gross error detection number of MAD and WS-MAD

Preprocessing methods	PRN19		PRN25		PRN38		PRN59	
	30	300	30	300	30	300	30	300
MAD	8	4	10	0	22	1	9	12
WS-MAD	17	9	16	7	41	6	30	16
Difference	9	5	6	7	19	5	21	4

As can be seen from Figs. 4 and 5 (a), (b), (c), and (d) plots and Table 3, more gross errors were detected by the WS-MAD method compared to the MAD gross error detection method.

Figure 4 shows that the clock bias frequency sequence diagrams for PRN19 and PRN25 satellites exhibit no discernible trends. The MAD preprocessing method successfully detects the majority of gross errors; however, it struggles to identify smaller gross errors. The WS-MAD strategy transforms the clock bias frequency data into distances between vector points and the center of a circle within a high-dimensional feature space. This transformation enhances the data's difference, thereby facilitating the detection of small gross errors. In the frequency sequence diagrams of the clock bias, the PRN38 and PRN59 satellites exhibit trend terms.

The MAD gross error detection adopts a fixed *m*-value. Due to the influence of data trend term, it is difficult for y_i deviating from *m*-value to detect gross error through distance constraint condition, which leads to poor gross error detection effect of MAD method. As a result, the MAD method yields poor performance in gross error detection. The WS-MAD strategy takes full account of the local characteristics of data points. By assigning higher weights to normal data, the weight assigned to gross error points is reduced. This weighting scheme enables the detection of gross errors that occur under different trends.

Figure 5 demonstrates a similar effect in detecting gross errors as Figure 4. However, in the case of PRN25 with a 300 s sampling interval, the MAD gross error detection fails to identify the presence of gross errors. The figure clearly illustrates the presence of gross errors in this frequency data. By successfully detecting the presence of gross errors, the WS-MAD strategy demonstrates the superiority of the WS-MAD algorithm.

To assess the viability of the proposed preprocessing algorithm for gross error rejection, we utilized clock bias frequency data from four satellites: PRN19, PRN25, PRN38, and PRN59. These data were preprocessed using both the MAD method and the WS-MAD method. Subsequently, the recovered original clock bias data underwent analysis for fitting and prediction, with the root-mean-square error (RMS) serving as the metric to evaluate the accuracy of both fitting and prediction. The RMS is calculated as follows:

$$\sigma=\sqrt{\frac{1}{n}\sum_{i=1}^{n}(\Delta\varepsilon_i)^2}\,, \tag{13}$$

where $\Delta\varepsilon_i$ is the difference between the fitted clock bias value and the true clock bias value, and n is the number of clock bias.

The fitting accuracies of the clock bias data of the four satellites after MAD and WS-MAD preprocessing at different sampling intervals are statistically presented in Tables 4 and 5.

Table 4. Statistics of fitting accuracy after MAD and WS-MAD preprocessing (30 s)

Preprocessing model	PRN19	PRN25	PRN38	PRN59
MAD, ns	0.171	0.094	0.545	0.514
WS-MAD, ns	0.164	0.088	0.513	0.482
Improvement, %	4.09%	6.38%	5.87%	6.23%

Table 5. Statistics of fitting accuracy after MAD and WS-MAD preprocessing (300 s)

Preprocessing model	PRN19	PRN25	PRN38	PRN59
MAD, ns	0.154	0.094	0.560	0.502
WS-MAD, ns	0.147	0.084	0.528	0.482
Improvement, %	4.55%	10.64%	5.71%	3.98%

The analysis of Tables 4 and 5 reveals that the fitting accuracy of the clock bias data for PRN19, PRN25, PRN38, and PRN59 satellites significantly improves when preprocessed using the WS-MAD method in comparison to the MAD method. Moreover, the effect of improving satellite clock fitting accuracy varies across different sampling intervals.

Among the satellites, PRN25 exhibits the most significant improvement with a 30 s sampling interval, as the fitting accuracy after WS-MAD preprocessing achieves 0.088 ns, representing a 6.83% enhancement over the MAD method. Conversely, PRN19 demonstrates the least improvement, with a fitting accuracy of 0.164 ns after WS-MAD preprocessing, showing a 4.09% improvement compared to the MAD method. The PRN38 and PRN59 satellites exhibit lifting accuracies of 5.87% and 6.23%, respectively. On average, the accuracy of the four satellites improves by 5.64%.

Among the data with a 300 s sampling interval, the PRN25 satellite demonstrates the most significant enhancement effect, achieving an improvement of 10.64%. Conversely, the PRN59 satellite exhibits the least enhancement effect, with only a 3.98% improvement. The PRN38 and PRN59 satellites exhibit enhancement accuracies of 5.71% and 3.98%, respectively. On average, the accuracy of the four satellites improved by 6.22%.

The gray model is used to model the clock bias data preprocessed by MAD and WS-MAD methods to forecast the satellite clock bias in the next 24h. Tables 6 and 7 show the statistics of four satellites under different sampling intervals

Table 6. Statistics of prediction accuracy after MAD and WS-MAD preprocessing (30 s)

Prediction/ns	PRN19	PRN25	PRN38	PRN59
M-GM(1,1)	2.498	1.036	2.581	2.191
WSM-GM(1,1)	2.247	0.863	2.120	2.002
Improvement, %	10.05%	16.70%	17.86%	8.63%

Table 7. Statistics of prediction accuracy after MAD and WS-MAD preprocessing (300 s)

Prediction/ns	PRN19	PRN25	PRN38	PRN59
M-GM(1,1)	2.921	1.008	2.517	2.095
WSM-GM(1,1)	2.465	0.902	2.235	1.906
Improvement, %	15.61%	10.52%	11.20%	9.02%

.

Tables 6 and 7 reveal that the prediction accuracy of the clock bias data for PRN19, PRN25, PRN38, and PRN59 satellites significantly improves when preprocessed using the WS-MAD method in comparison to the MAD method.

Among the data with a 30 s sampling interval, the PRN38 satellite exhibits the most significant improvement effect, with the prediction accuracy reaching 2.120 ns after WS-MAD preprocessing, representing a 16.70% improvement compared to the MAD method. Conversely, the PRN59 satellite shows the least improvement effect, with the prediction accuracy after WS-MAD preprocessing reaching 2.002 ns, indicating an 8.63% improvement compared to the MAD method. The PRN19 and PRN25 satellites achieve prediction accuracies of 10.05% and 16.70%, respectively. On average, the accuracy of the four satellites improves by 13.31%.

Among the data with a 300 s sampling interval, the PRN19 satellite demonstrates the most significant enhancement effect, achieving an improvement of 15.61%. Conversely, the PRN59 satellite exhibits the least enhancement effect, with only a 9.02% improvement. The PRN38 and PRN59 satellites exhibit enhancement accuracies of 10.52% and 11.20%, re-

spectively. On average, the accuracy of the four satellites improved by 11.59%.

3.2. Experiment 2

Experiment 1 confirms that the proposed preprocessing algorithm effectively detects minor gross errors in smooth frequency series and more gross errors in frequency data with floating trend terms. Due to the uncertainty of a single satellite, it is not possible to judge the enhancement effect of the WS-MAD preprocessing method on satellites with different orbits and different clock types. To address this, we selected the clock bias data of BDS-3 MEO PRN19-PRN30, IGSO PRN38-PRN40, and GEO PRN59-PRN60 satellites for subsequent experimental analysis. Tables 8 and 9 provide a summary of the fitting accuracies of the clock bias data from 17 satellites after MAD and WS-MAD preprocessing, respectively, considering different sampling intervals. Figure 6 illustrates the improvement in fitting accuracy values for each satellite based on WS-MAD preprocessing at 30 s and 300 s sampling intervals.

Table 8. Statistical values of fitting accuracy for different orbital satellite clocks based on MAD and WS-MAD preprocessing (30 s)

PRN	MAD	WS-MAD	Accuracy improvement	Mean accuracy improvement	Satellite clock type	Track type
PRN 19	1.975e-10	1.780e-10	9.87%	8.30%	rubidium clock	MEO
PRN 20	1.827e-10	1.657e-10	9.30%			
PRN 21	2.419e-10	2.318e-10	4.18%			
PRN 22	2.343e-10	2.192e-10	6.44%			
PRN 23	0.570e-10	0.528e-10	7.37%			
PRN 24	0.926e-10	0.809e-10	12.63%			
PRN 25	0.554e-10	0.354e-10	9.75%	15.04%	hydrogen clock	
PRN 26	0.814e-10	0.610e-10	25.06%			
PRN 27	0.144e-10	0.126e-10	12.50%			
PRN 28	0.901e-10	0.769e-10	14.65%			
PRN 29	1.053e-10	0.906e-10	13.96%			
PRN 30	0.938e-10	0.804e-10	14.29%			
PRN 38	1.444e-10	1.311e-10	9.21%	8.58%	hydrogen clock	IGSO
PRN 39	1.489e-10	1.378e-10	7.45%			
PRN 40	1.687e-10	1.534e-10	9.07%			
PRN 59	6.310e-10	6.055e-10	4.04%	5.27%	hydrogen clock	GEO
PRN 60	3.725e-10	3.483e-10	6.50%			

Table 9. Statistical values of fitting accuracy for different orbital satellite clocks based on MAD and WS-MAD preprocessing (300 s).

PRN	MAD	WS-MAD	Accuracy improvement	Mean accuracy improvement	Satellite Clock Type	Track type
PRN 19	2.081e-10	1.750e-10	15.91%	13.40%	rubidium clock	MEO
PRN 20	1.896e-10	1.522e-10	19.73%			
PRN 21	2.377e-10	2.117e-10	10.94%			
PRN 22	2.220e-10	1.933e-10	12.93%			
PRN 23	0.561e-10	0.515e-10	8.20%			
PRN 24	0.869e-10	0.759e-10	12.66%			
PRN 25	0.506e-10	0.458e-10	9.49%	16.01%	hydrogen clock	
PRN 26	0.912e-10	0.751e-10	17.62%			
PRN 27	1.416e-10	1.230e-10	13.14%			
PRN 28	0.901e-10	0.744e-10	17.43%			
PRN 29	1.108e-10	0.927e-10	16.34%			
PRN 30	0.958e-10	0.747e-10	22.03%			
PRN 38	1.518e-10	1.347e-10	11.26%	12.24%	hydrogen clock	IGSO
PRN 39	1.546e-10	1.345e-10	13.00%			
PRN 40	1.845e-10	1.615e-10	12.47%			
PRN 59	6.469e-10	6.125e-10	5.32%	5.31%	hydrogen clock	GEO
PRN 60	3.787e-10	3.584e-10	5.29%			

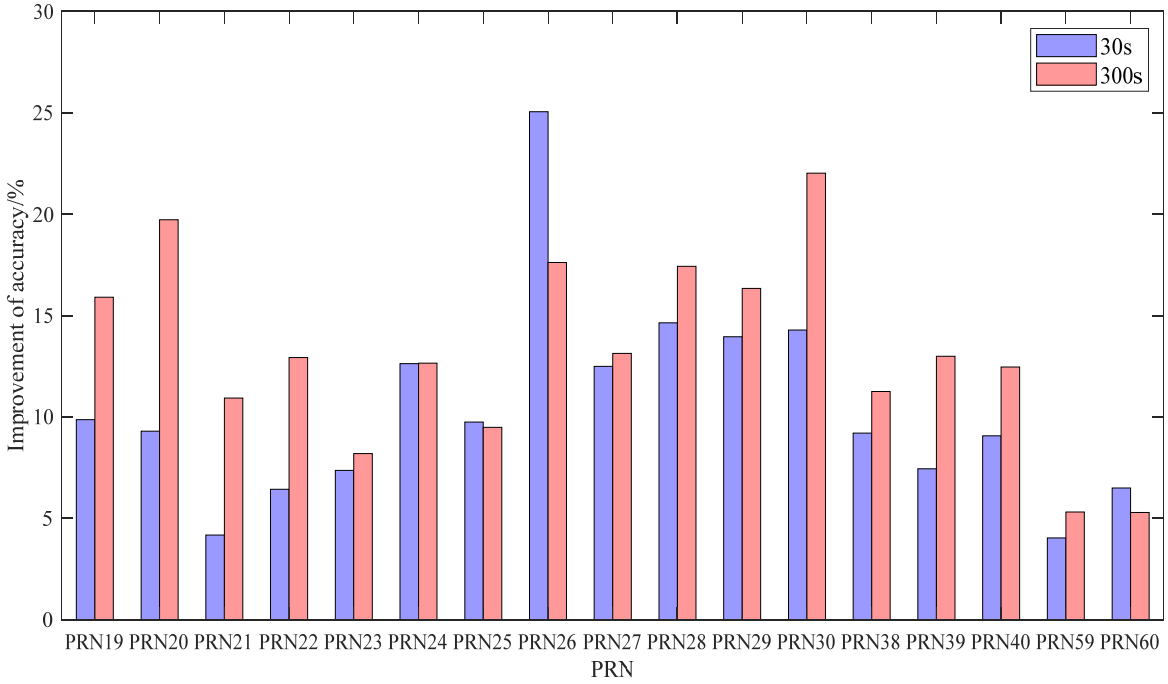

Fig. 6. Improvement in fitting accuracy of satellites in different orbits based on WS-MAD preprocessing.

Table 8 presents the statistical values of the fitting accuracy for the two preprocessing methods at a 30 s sampling interval. In general, the MEO-orbiting PRN26 satellite, equipped with a hydrogen clock, exhibits the highest enhancement accuracy, achieving a remarkable improvement of 25.06%. Conversely, the PRN59 satellite in the GEO orbit, equipped with a hydrogen clock, demonstrates the lowest improvement accuracy, reaching only 4.04%. Considering different orbit types, the average enhancement accuracy for MEO, IGSO, and GEO satellites is 11.67%, 8.58%, and 5.27%, respectively. Among them, MEO satellites exhibit the highest enhancement accuracy, followed by IGSO satellites, while GEO satellites show the lowest enhancement accuracy. This indicates that the proposed preprocessing method effectively enhances the quality of clock bias data for MEO and IGSO satellites. Focusing solely on MEO satellites, the improvement accuracy of the hydrogen clock is 15.04%, whereas the rubidium clock achieves an improvement accuracy of 8.30%. Notably, the hydrogen clock exhibits a higher improvement accuracy compared to the rubidium clock.

Table 9 presents the statistical values of the fitting accuracy for the two preprocessing methods at a 300 s sampling interval. Similarly to the 30 s sampling interval, the hydrogen clock in the MEO orbit demonstrates superior enhancement accuracy compared to the rubidium clock. Among the different orbit types, MEO satellites exhibit the highest average enhancement accuracy of 14.71%, followed by IGSO satellites at 12.24%, while GEO satellites show the lowest enhancement accuracy of 5.31%. In general, the PRN30 satellite, equipped with a hydrogen clock, achieves the highest improvement accuracy of 22.03%. Conversely, the PRN60 satellite in the GEO orbit, equipped with a hydrogen clock, exhibits the lowest improvement accuracy, reaching only 5.29%.

Comparing Tables 8 and 9, the proposed preprocessing algorithm is more effective in improving the fitting accuracy of the clock bias data at 300 s sampling interval than that of the clock bias data at 30 s sampling interval in terms of the three orbital types. Figure 6 illustrates that, with the exception of PRN25, PRN26, and PRN60 satellites, the improvement in fitting accuracy for the remaining satellite clocks is greater at the 300 s sampling interval compared to the 30 s sampling interval data.

To examine the prediction of clock bias data after WS-MAD preprocessing, we employ the gray model (GM (1,1)) and the quadratic polynomial model. These models are utilized to represent the clock bias data after preprocessing by MAD and WS-MAD, respectively, and to forecast the clock bias for the upcoming 24 hours. The accuracy of the forecast results is assessed through the root mean square error (RMS), where the precise clock bias value corresponding to the forecast time period serves as the reference true value. Tables 10 and 11 present the prediction accura-

cy of 17 satellites at 30 and 300 s sampling intervals following MAD and WS-MAD preprocessing when utilizing the gray model to forecast the 24-hour period. Tables 12 and 13 show the prediction accuracy of the quadratic polynomial model for 17 satellites at 30 and 300 s sampling intervals after MAD and WS-MAD preprocessing for 24h duration.

Table 10. Statistical values of 24-h duration accuracy of gray model-based forecasts for satellite clocks in different orbits (30 s)

PRN	M-GM(1,1), ns	WSM-GM(1,1), ns	Accuracy improvement	Mean accuracy improvement	Satellite clock type	Track type
PRN 19	0.668	0.497	25.60%	11.90%	rubidium clock	MEO
PRN 20	3.358	3.134	6.67%			
PRN 21	7.756	6.752	12.94%			
PRN 22	3.320	2.992	9.88%			
PRN 23	5.518	5.102	7.54%			
PRN 24	2.593	2.367	8.72%			
PRN 25	0.415	0.354	14.70%	19.34%	hydrogen clock	
PRN 26	0.621	0.525	15.46%			
PRN 27	0.360	0.300	16.67%			
PRN 28	2.998	2.370	20.95%			
PRN 29	0.547	0.397	27.42%			
PRN 30	0.614	0.486	20.85%			
PRN 38	2.226	1.996	10.33%	13.20%	hydrogen clock	IGSO
PRN 39	0.822	0.690	16.06%			
PRN 40	3.439	3.060	11.02%			
PRN 59	2.721	2.518	7.46%	7.92%	hydrogen clock	GEO
PRN 60	2.757	2.526	8.38%			

Table 11. Statistical values of 24-h duration accuracy of gray model-based forecasts for satellite clocks in different orbits (300 s)

PRN	M-GM(1,1), ns	WSM-GM(1,1), ns	Accuracy improvement	Mean accuracy improvement	Satellite clock type	Track type
PRN 19	0.627	0.406	35.25%	14.36%	rubidium clock	MEO
PRN 20	3.401	3.072	9.67%			
PRN 21	8.086	7.018	13.21%			
PRN 22	3.316	2.946	11.16%			
PRN 23	5.438	4.968	8.64%			
PRN 24	2.405	2.207	8.23%			
PRN 25	0.424	0.314	16.04%	19.29%	hydrogen clock	
PRN 26	0.784	0.607	22.58%			
PRN 27	0.460	0.375	18.48%			
PRN 28	2.830	2.475	12.54%			
PRN 29	0.668	0.488	26.95%			
PRN 30	0.548	0.443	19.16%			
PRN 38	2.313	2.054	11.20%	12.30%	hydrogen clock	IGSO
PRN 39	0.798	0.681	14.66%			
PRN 40	3.424	3.046	11.04%			
PRN 59	2.660	2.332	12.33%	11.11%	hydrogen clock	GEO
PRN 60	2.721	2.452	9.89%			

Table 10 shows the accuracy statistical values of the 24-h forecast using the gray model after the two preprocessing methods at 30-s sampling interval. In general, the MEO satellite PRN29, equipped with a hydrogen clock, demonstrates the highest improvement accuracy at 27.42%, while the MEO satellite PRN20, equipped with a rubidium clock, exhibits the lowest improvement accuracy at only 6.67%. Considering different orbit types, the average enhancement accuracies for MEO, IGSO, and GEO satellites are 15.62%, 13.20%, and 7.92%, respectively. MEO satellites exhibit the highest enhancement accuracies, followed by IGSO satellites, while GEO satellites show the lowest enhancement accuracies. This indicates that the proposed preprocessing method effectively enhances the quality of clock bias data for MEO and IGSO satellites. Focusing solely on MEO orbit satellites, the improvement accuracy for the hydrogen clock is 19.34%, whereas for the rubidium clock, it is 11.90%. Moreover, the average improvement accuracy for the hydrogen clock surpasses that of the rubidium clock.

Table 11 shows the accuracy statistics of the 24-h forecast using the gray model after the two preprocessing methods for the 300-s sampling interval. Similarly to the 30-s sampling interval, the average improvement accuracy of the MEO orbit's hydrogen clock surpasses that of the rubidium clock. Across different orbital types, the average improvement accuracies for MEO, IGSO, and GEO satellites are 16.83%, 12.30%, and 11.11%, respectively. MEO satellites exhibit the highest improvement accuracy, followed by IGSO satellites, while GEO satellites demonstrate the lowest improvement accuracy. Overall, the satellite PRN19 equipped with a rubidium clock exhibits the highest improvement accuracy at 35.25%, while the MEO satellite PRN24 equipped with a rubidium clock demonstrates the lowest improvement accuracy, merely 8.23%. Comparing Tables 10 and 11, for MEO and GEO satellites, the WSMAD method provides a greater enhancement with 300 s clock bias data. And for the IGSO, the WSMAD method is better at boosting the clock bias data of 30 s than the clock bias data of 300 s.

Table 12. Statistical values of 24-h duration accuracy of quadratic polynomial model-based forecasts for satellite clocks in different orbits (30 s)

PRN	M-QP, ns	WSM-QP, ns	Accuracy improvement	Mean accuracy improvement	Satellite clock type	Track type
PRN 19	2.328	1.978	15.03%	13.57%	rubidium clock	MEO
PRN 20	1.766	1.547	10.87%			
PRN 21	1.479	1.324	10.48%			
PRN 22	1.595	1.507	5.52%			
PRN 23	0.691	0.599	13.31%			
PRN 24	1.216	0.897	26.23%			
PRN 25	0.415	0.360	13.25%	19.91%	hydrogen clock	
PRN 26	1.357	1.025	24.47%			
PRN 27	1.685	1.452	13.83%			
PRN 28	0.609	0.468	23.15%			
PRN 29	1.696	1.426	15.92%			
PRN 30	1.106	0.787	28.84%			
PRN 38	1.541	1.398	9.28%	9.97%	hydrogen clock	IGSO
PRN 39	2.092	1.944	7.07%			
PRN 40	2.244	1.940	13.55%			
PRN 59	4.705	4.342	7.72%	7.43%	hydrogen clock	GEO
PRN 60	2.647	2.458	7.14%			

Table 13. Statistical values of 24-h duration accuracy of quadratic polynomial model-based forecasts for satellite clocks in different orbits (300 s)

PRN	M-QP, ns	WSM-QP, ns	Accuracy improvement	Mean accuracy improvement	Satellite clock type	Track type
PRN 19	2.548	1.965	15.03%	12.35%	rubidium clock	MEO
PRN 20	1.623	1.234	10.87%			
PRN 21	1.581	1.351	14.55%			
PRN 22	1.595	1.436	9.97%			
PRN 23	0.708	0.654	7.63%			
PRN 24	1.234	1.036	16.05%			
PRN 25	0.484	0.406	16.12%	21.67%	hydrogen clock	
PRN 26	1.482	0.983	33.67%			
PRN 27	1.579	1.328	15.90%			
PRN 28	0.524	0.402	23.28%			
PRN 29	1.302	1.097	15.75%			
PRN 30	1.199	0.896	25.27%			
PRN 38	1.462	1.320	9.71%	8.62%	hydrogen clock	IGSO
PRN 39	2.333	2.192	6.04%			
PRN 40	2.036	1.830	10.12%			
PRN 59	4.958	4.620	7.72%	7.30%	hydrogen clock	GEO
PRN 60	1.841	1.673	7.14%			

Table 12 shows the accuracy statistics values of the 24-h forecast using the quadratic polynomial model after the two preprocessing methods at 30-s sampling interval. In general, the MEO satellite PRN30, equipped with a hydrogen clock, exhibits the highest improvement accuracy at 28.84%, while the MEO satellite PRN22, equipped with a rubidium clock, demonstrates the lowest improvement accura-

cy, which is only 5.52%. Considering different orbital types, the average enhancement accuracies for MEO, IGSO, and GEO satellites are 16.74%, 9.97%, and 7.43%, respectively. MEO satellites demonstrate the highest enhancement accuracy, followed by IGSO satellites, while GEO satellites exhibit the lowest enhancement accuracy. Examining solely the MEO orbit satellites, the enhancement accuracy for the hydrogen clock is 19.91%, while for the rubidium clock, it is 13.57%. Moreover, the average enhancement accuracy for the hydrogen clock surpasses that of the rubidium clock.

Table 13 shows the accuracy statistics of the 24-h forecast using a quadratic polynomial model after the two preprocessing methods for the 300-s sampling interval. Similarly to the 30-second sampling interval, the average improvement accuracy of the MEO orbit's hydrogen clock surpasses that of the rubidium clock. Across different orbital types, the average improvement accuracies for MEO, IGSO, and GEO satellites are 17.01%, 8.62%, and 7.30%, respectively. MEO satellites exhibit the highest improvement accuracy, followed by IGSO satellites, while GEO satellites demonstrate the lowest improvement accuracy. Overall, the satellite PRN26 equipped with a hydrogen clock exhibits the highest improvement accuracy at 33.67%, whereas the IGSO satellite PRN39, also equipped with a hydrogen clock, demonstrates the lowest improvement accuracy of only 6.04%.

The average forecast boosting accuracy of the proposed preprocessing algorithm for clock bias data with a 300-second sampling interval is comparable to that of the clock bias data with a 30-second sampling interval for all three orbital types when comparing Tables 12 and 13.

4. CONCLUSIONS

This paper proposes a method for detecting gross errors in satellite clock bias data, combining weighted SVDD with corrected MAD. Precision clock bias data with sampling intervals of 30 s and 300 s from GFZ are selected for the experiment. Firstly, based on the modified MAD and WS-MAD methods, the gross error detection is carried out on four satellite clocks with different characteristics of clock bias frequency data. The effectiveness and feasibility of detecting clock bias gross errors are verified by evaluating the fitting accuracy and forecasting accuracy. Additionally, the impact of the WS-MAD method on improving the fitting accuracy and forecasting accuracy for satellites with different orbits and clock types is investigated.

The experimental results demonstrate that the WS-MAD method outperforms the MAD gross error detection method in detecting smaller gross error points in clock bias data with varying sampling intervals. Moreover, it exhibits a superior detection effect for clock bias data with floating trend terms. The WS-MAD method is better than the MAD gross error detection method in both fitting accuracy and forecasting accuracy. Through an analysis of the fitting accuracy and forecasting accuracy of satellites with varying orbits and clock types, it is evident that the WS-MAD method exhibits higher boosting accuracy for MEO and IGSO satellites compared to GEO orbit satellites. Among satellites in the same orbit, hydrogen clocks demonstrate greater enhancement accuracy than rubidium clocks. The preprocessing algorithm proposed in this paper enriches the quality control method of satellite clock bias data to a certain extent, which can be used as a reference for the users of satellite clock performance analysis, precision positioning, and clock bias prediction.

FUNDING

This work was supported by ongoing institutional funding. No additional grants to carry out or direct this particular research were obtained.

CONFLICTS OF INTEREST

The authors declare that they have no conflicts of interest.

REFERENCES

1. Yang, Y.F., Pan, X., Qing, C.X., Mei, C.S., & Lai, Z.L., Detection and repair of outliers in BDS satellite clock offset based on semiparametric mean drift model, *Chinese Journal of Scientific Instrument*, 2020, no. 8, pp. 47-54.
2. He, S., Liu, J., Zhu, X., Dai, Z., & Li, D., Research on modeling and predicting of BDS-3 satellite clock bias using the LSTM neural network model, *GPS Solutions*, 2023, vol. 27, no. 3, 108. https://doi.org/2023.10/s1007-10291-023-01451
3. Feng, S.L., Study on the methods of data preprocessing and performance analysis for atomic clocks, *M.Sc. Thesis*, Henan: Information Engineering University, 2009.
4. Zhou, S., Hu, X., Liu, L. et al., Applications of two-way satellite time and frequency transfer in the BeiDou navigation satellite system, *Science China Physics, Mechanics and Astronomy*, 2016, vol. 59, pp. 1-9. https://doi.org/10.1007/s11433-016-0185-6

5. Guo, J.S., Time scale steering in UTC (NIM), Beijing: Beijing University of Technology, 2013.
6. Ghaderpour, E. and Vujadinovic, T., The potential of the least-squares spectral and cross-wavelet analyses for near-real-time disturbance detection within unequally spaced satellite image time series, *Remote Sensing*, 2020, vol. 12, no. 15, 2446. https://doi.org/10.3390/rs12152446
7. Riley, W. and Howe, D., Handbook of Frequency Stability Analysis, Special Publication (NIST SP), National Institute of Standards and Technology, Gaithersburg, MD, 2008.
8. Wang, W., Xu, F., and Wang, Y.P., A preprocess method for gross error detection based on wavelet analysis, *Journal of Geodesy and Geodynamics*, 2021, 41, pp. 623-627.
9. Fang, S.S., Research of GPS Satellite Clock Error Integrity Monitoring and Algorithm Implementation, *M.Sc. Thesis*, Fuxin: Liaoning Technical University, 2009.
10. Wei, D.K., Study on the Satellite Clock Bias Forecast Model, *M.Sc. Thesis*, Xi'an: Liaoning Technical University, 2009.
11. Zhang, Q., Han, S., Du, L., and Gui, Q., Bayesian methods for outliers detection and estimation in clock offset measurements of satellite-ground time transfer, Geomatics and Information Science of Wuhan University, 2016, vol. 41, no. 6, pp. 772-777.
12. Xue, H., Xu, T., Nie, W., Yang, Y., & Ai, Q., An enhanced prediction model for BDS ultra-rapid clock offset that combines singular spectrum analysis, robust estimation and gray model, *Measurement Science and Technology*, 2021, vol. 32, no. 10, 105002. https://doi.org/10.1088/1361-6501/abfcec
13. Zheng, Y., Wang, S., and Chen, B., Robust one-class classification with support vector data description and mixed exponential loss function, *Engineering Applications of Artificial Intelligence*, 2023, vol. 122, 106153. https://doi.org/10.1016/j.engappai.2023.106153
14. Feng, Z., Wang, Z., Liu, X., and Li, J., Rolling bearing performance degradation assessment with adaptive sensitive feature selection and multi-strategy optimized SVDD, *Sensors*, 2023, vol. 23, no. 3, 1110. https://doi.org/10.3390/s23031110
15. Wang, Z.J., Multimode Industrial Process Modeling and Monitoring Based on Statistical Machine Learning, *Ph.D. Thesis*, Wuhan: Huazhong University of Science and Technology, 2021.
16. Zhong, G., Xiao, Y., Liu, B., Zhao, L., and Kong, X., Pinball loss support vector data description for outlier detection, *Applied Intelligence*, 2022, vol. 52, no. 14, pp. 16940-16961. https://doi.org/10.1007/s10489-022-03237-5
17. Li, H., Wang, H., and Fan, W., Multimode process fault detection based on local density ratio-weighted support vector data description, *Industrial & Engineering Chemistry Research*, 2017, vol. 56, no. 9, pp. 2475-2491. https://doi.org/10.1021/acs.iecr.6b03306
18. Wang, Z., Yang, W., Zhang, H., and Zheng, Y., SPA-based modified local reachability density ratio wSVDD for nonlinear multimode process monitoring, *Complexity*, 2021, pp. 1-15. https://doi.org/10.1155/2021/5517062
19. Breunig, M.M., Kriegel, H.P., Ng, R.T., and Sander, J., LOF: identifying density-based local outliers, Proceedings of the 2000 *ACM SIGMOD International Conference on Management of Data*, 2000, May, pp. 93-104. https://doi.org/10.1145/342009.335388
20. Xiao, Y., Wang, H., Zhang, L., and Xu, W., Two methods of selecting Gaussian kernel parameters for one-class SVM and their application to fault detection, *Knowledge-Based Systems*, 2014, vol. 59, pp. 75-84. https://doi.org/10.1016/j.knosys.2014.01.020
21. Wang, W., Wang, Y., Yu, C., Xu, F., and Dou, X., Spaceborne atomic clock performance review of BDS-3 MEO satellites, *Measurement*, 2021, vol. 175, 109075. https://doi.org/10.1016/j.measurement.2021.109075
22. Geng, T., Jiang, R., Lv, Y., and Xie, X., Analysis of BDS-3 onboard clocks based on GFZ precise clock products, *Remote Sensing*, 2022, vol. 14, 1389. https://doi.org/10.3390/rs14061389
23. He, L., Zhou, H., Zhu, S., and Zeng, P., An improved QZSS satellite clock offsets prediction based on the extreme learning machine method, *IEEE Access*, 2020, vol. 8, pp. 156557-156568. https://doi.org/10.1109/ACCESS.2020.3019941
24. Huang, B., Yang, B., Li, M., Guo, Z., Mao, J., and Wang, H., An improved method for MAD gross error detection of clock error, Geomatics and Information Science of Wuhan University, 2022, vol. 47, no. 5, pp. 747-752. https://doi.org/10.13203/j.whugis20190430
25. Xu, Z.Y., The Evaluation of IGS Real-Time Product and Research on Positioning Method of Real-Time PPP, *M.Sc. Thesis*, Beijing: China University of Geosciences, 2021.
26. Lv, D., Liu, G., Ou, J., Wang, S., and Gao, M., Prediction of GPS satellite clock offset based on an improved particle swarm algorithm optimized BP neural network, *Remote Sensing*, 2022, vol. 14, no. 10, 2407. https://doi.org/10.3390/rs14102407.